8th U. S. National Combustion Meeting
Organized by the Western States Section of the Combustion Institute
and hosted by the University of Utah
May 19-22, 2013

Quantitative Infrared Image Analysis Of Simultaneous Upstream and Downstream Microgravity Flame Spread over Thermally-Thin Cellulose in Low Speed Forced Flow

S.L. Olson[1], J. R. Lee[2], O. Fujita[3], M. Kikuchi[4], and T. Kashiwagi[5]

[1]NASA Glenn Research Center, Cleveland, OH
[2]QinetiQ North America, Cleveland, OH
[3]Hokkaido University, Sapporo, Japan
[4]JAXA, Tsukuba, Japan
[5] National Institute of Standards and Technology, Gaithersburg, MD

The effect of low velocity forced flow on microgravity flame spread is examined using quantitative analysis of infrared video imaging. The objective of the quantitative analysis is to provide insight into the mechanisms of flame spread in microgravity where the flame is able to spread from a central location on the fuel surface, rather than from an edge. Surface view calibrated infrared images of ignition and flame spread over a thin cellulose fuel were obtained along with a color video of the surface view and color images of the edge view using 35 mm color film at 2 Hz. The cellulose fuel samples were mounted in the center of a 12 cm wide by 16 cm tall flow duct and were ignited in microgravity using a straight hot wire across the center of the 7.5 cm wide by 14 cm long samples. Four cases, at 1 atm. 35%O_2 in N_2, at forced flows from 2 cm/s to 20 cm/s are presented here. This flow range captures flame spread from strictly upstream spread at low flows, to predominantly downstream spread at high flow. Surface temperature profiles are evaluated as a function of time, and temperature gradients for upstream and downstream flame spread are measured. Flame spread rates from IR image data are compared to visible image spread rate data. IR blackbody temperatures are compared to surface thermocouple readings to evaluate the effective emissivity of the pyrolyzing surface. Preheat lengths and pyrolysis lengths are evaluated both upstream and downstream of the central ignition point. A surface energy balance estimates the net heat flux from the flame to the fuel surface along the length of the fuel. Surface radiative loss and gas-phase radiation from soot are measured relative to the net heat feedback from the flame. At high surface heat loss relative to heat feedback, the downstream flame spread does not occur.

[1] Corresponding Author: Sandra L. Olson, NASA Glenn Research Center, 21000 Brookpark Rd. m.s. 77-5, Cleveland, OH 44135. Phone (216) 433-2859, Fax (216) 433-8050, email Sandra.L.Olson@NASA.gov

1. Introduction

Microgravity flame spread over thin solid fuels has been a subject of considerable research over the past 30 years, and there have been significant advances in our understanding of the mechanisms of flame spread in microgravity [Ross (2001), Fernandez-Pello]. Notably, the roles of solid-phase radiative loss [T'ien] and oxygen transport [Olson (1991)] on the microgravity extinction limits of solid fuels have been well established. Quantitative analysis of surface temperature profiles and net heat flux from the flame to the fuel has been challenging even in normal gravity experiments [Hirano& Sato, Quintiere]. Researchers have used thermocouples [Hirano et al., Cordova et al.] or holographic interferometry [Ito& Kashiwagi] in normal gravity, but only a few microgravity tests have attempted to measure surface temperatures or heat flux [Bhattacharjee et al., Olson et al. (2001), Olson et al (2004)]. Numerical models have been used to predict the net heat flux from the flame to the solid fuel [Ferkul & T'ien, Di Blasi, Prasad et al., Nakamura et al., Kumar et al.].

There have been limited studies using infrared cameras in microgravity [Sanchez-Tarifa & Lazaro, Ross & Miller, Feier et al., Kleinhenz et al.], most of which were of limited quantitative utility because of the early IR camera's 8 bit dynamic range. However, more advanced cameras have increased the bit depth, which improves the dynamic range enough to make the cameras useful for imaging surface heat up and pyrolysis during combustion experiments. In this work we present surface IR image results from microgravity combustion of cellulose fuels in different oxygen and flow environments. A previous paper [Prasad et al.] reported on visible flame spread results and compared the results to model predictions. The infrared surface temperature data reported here can provide added depth to the model comparisons.

2. Experimental Method

The experimental hardware, shown conceptually in Figure 1, is described in [Prasad et al.], and consisted of a flow duct inside a sealed chamber which was filled with 21%, 35%, or 50% oxygen in nitrogen at 1 atmosphere pressure. The flow duct provided a uniform flow of 2-20 cm/s past the fuel sample. The fuel samples were 60 mg/cm^2 cellulose 7.5 cm wide and 14 cm long. They were ignited with a straight hot wire across the center of the sample (7 cm of fuel upstream and downstream of the igniter) starting at time=0s (represented by the yellow dot in Figure 1). The flame was established by 2 seconds, so the data analysis begins at 2 seconds. At the end of the microgravity time, a solenoid valve opens and $CO_2$is blown into the duct to extinguish the flame.

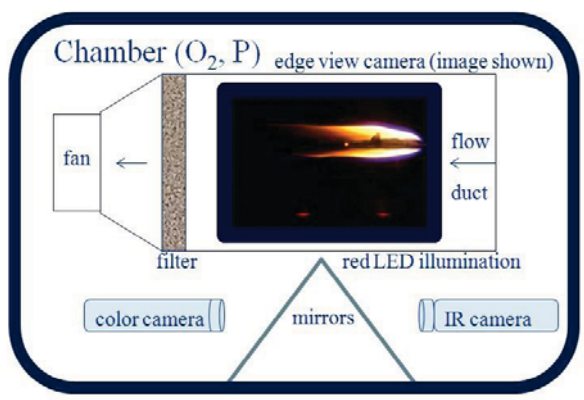

Figure 1: Conceptual schematic of experiment. Edge view image of the sample and flame in the flow duct. The central igniter is represented by the yellow dot. Two surface view cameras are shown.

The infrared camera used in the tests was a 12 bit FLIR Systems, Inc. Prism DS™ with a 50 mm lens. A 200 nm bandwidth 'flame filter' centered at 3.8 μm was used to remove most of the gas-phase radiation from CO2 and H2O. The surface temperature calibration was performed with a

calibrated Micron™ black body over the camera's operating range of 150°C to 770°C including the optical path elements (lens, calcium fluoride window, zinc sulfide window, 2 mirrors). A 10 pixel diameter area of the image was averaged to obtain the black body temperature to pixel level calibration. The accuracy of the black body surface temperatures is ±20°C, and the spatial resolution was 0.3 mm per pixel. The IR camera image was 244 x 320 pixels, and the field of view was 7.5 cm wide by 10 cm long. The infrared images were analyzed using Tracer™ and Thermacam Researcher™ software. [2]

A 35 mm color film camera was used to image the edge view of the flame during the test at ~ 2 frames per second, and a front view standard color video camera was used to image the surface view of the flame and fuel burning during the test. Type K thermocouples (0.005 cm diameter bare wire) were sewn into each sample to record the surface temperatures. The surface temperatures are used to compare to the black body temperature readings in order to get information on the fuel emissivity as it heats up and begins to pyrolyze. The surface thermocouple beads were located along the sample centerline at upstream locations +4 cm, +2 cm, 0 cm, and downstream -2 cm, all relative to the igniter location.

3. Results

3.1 Flame Images

Four tests at 35% oxygen molar percent at 2, 5, 10, and 20 cm/s forced flow velocities are shown in Figure 2. The edge view and surface view visible color images are

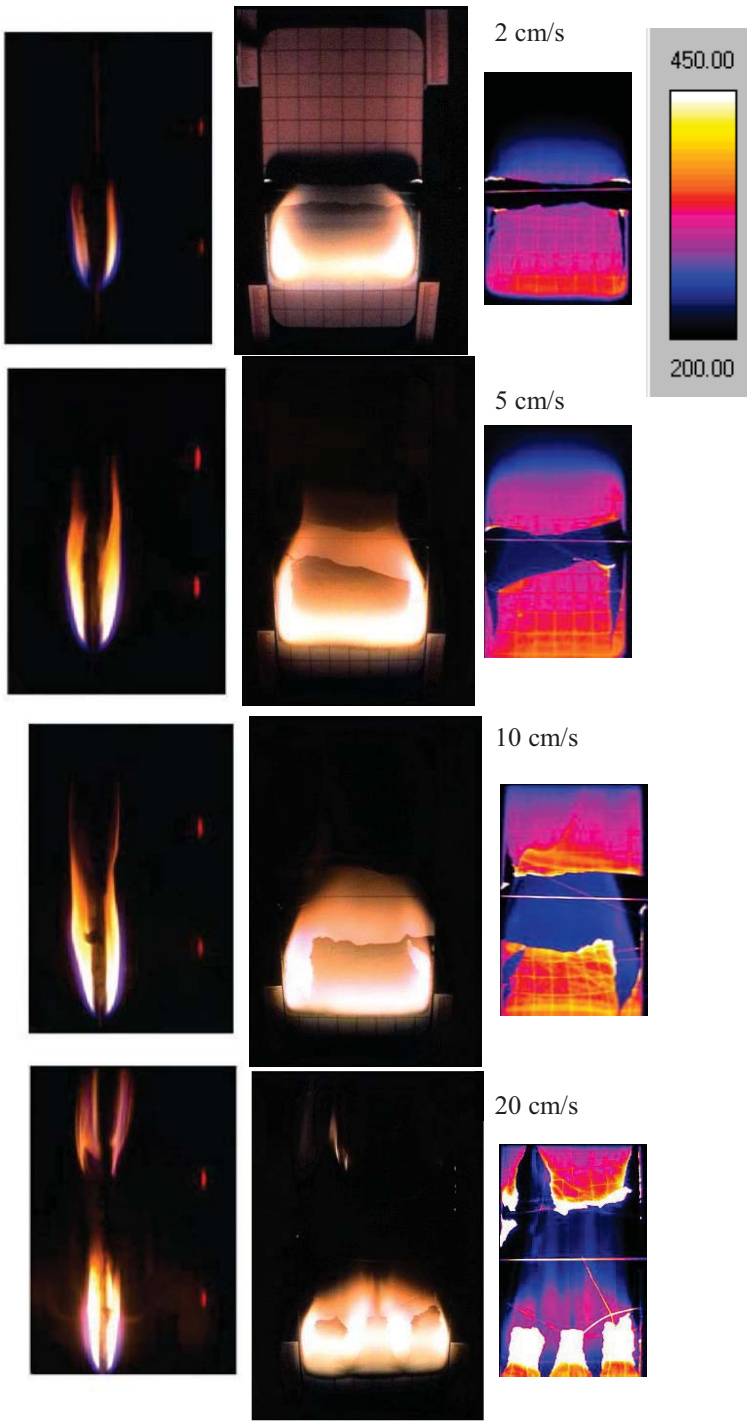

Figure 2: Visible edge view and front view images and IR front view images of the flame at the end of the drop. Times are not exact due to different framing rates. Flow velocities are as indicated. Flow is from bottom to top. IR view is mirror image of visible camera view.

[2]™ Reference herein to any specific commercial product, process, or service by trade name, trademark, manufacturer, or otherwise, does not necessarily constitute or imply its endorsement, recommendation, or favoring by the United States Government or any agency thereof or its contractors or subcontractors.

shown along with the surface infrared image, which has a smaller field of view than the color image. These images are all from the end of the drop test, although the timing is not exact due to different framing rates of the cameras. The printed grid on the sample is 1 cm square. It appears lighter in the infrared because its emissivity is higher than the pristine cellulose fuel. There is a horizontal igniter wire in the front view images. Red LEDs used to illuminate the sample are visible in the edge views. Very thin thermocouple wires are also present, and visible in some IR images. The flame spread is reasonably two dimensional since the sample is wide enough and the ignition is uniform across the fuel width. The IR color temperature legend is also shown.

The side view color images show the flame transitioning from a strictly upstream flame spread (2 cm/s) to two completely separate flames (20 cm/s). The sooting increases as the flow increases, and the flame standoff decreases with increasing flow. At 10 cm/s, a luminous upstream flame is visible in the edge view. This luminous flame fades as it extends downstream, and a kink in the flame shape is observed in the edge view near the location of the downstream fuel burnout edge. The outer blue halo flame fades before the kink, but there is a very faint blue inner flame visible in the left edge view flame that appears to be the beginning of a flame base attaching to the upstream edge of the downstream flame. The rest of the flame above the downstream side of the *fuel has a large standoff distance and appears to still be an extension of the upstream flame. This is* in contrast to the downstream flame fully separated from an upstream flame observed at 20 cm/s flow.

The surface color view images show that while the upstream leading edge of the flame is 2D, there are 3D soot structures occurring in the flame. At 2 cm/s, the sooting along the edges of the fuel is most pronounced. The downstream pyrolysis front is very flat. At 5 cm/s the sooting extends downstream over the downstream fuel, but in a pinched off funnel shape. The downstream burnout is fairly flat, and the pyrolysis front is also flat. This funnel is still present at 10 cm/s but appears to be longer. The downstream burnout is farther from the igniter wire. At 20 cm/s, the upstream flame has 3 soot lobes at the leading edge, with a large gap between the upstream burnout and downstream burnout. The downstream flame begins to show some independent sooting.

The IR images show the fairly 2D thermal structure of the pyrolizing fuel surface even up to 10 cm/s. Exothermic char oxidation that is a clear indication of a downstream flame base is clearly present in the 20 cm/s image, and is beginning to show at 10 cm/s with a slight saturated glow at the burnout. At 2 cm/s and 5 cm/s the only downstream exothermic char oxidation is at the fuel edges. It may be that the flame there would continue to spread given longer times and larger separation from the upstream flame. The fuel cracking late in the test does disrupt the symmetry of the fuel, and fuel distortion disturbs the flow somewhat. The gas-phase sooting increases in intensity in the burnout gap as flow increases. It is very strong in the upstream 20 cm/s flame.

Figure 3 shows the surface view of the initial sample (Fig. 3a), and the burned samples after the flame is extinguished (Figs.3b-3e) for each flow case. The infrared camera field of view is less than the total sample length, as shown in Figure 3a. Some of the pyrolyzed fuel has been blown away during the CO_2 suppression at the end of the microgravity time. As can be seen the upstream flames (bottom of the images) have propagated nearly to the edge of the fuel by the 20 cm/s case. The downstream fuel is also fully charred for 20 cm/s. However, at 2, 5, and even 10 cm/s much of the downstream fuel remains.

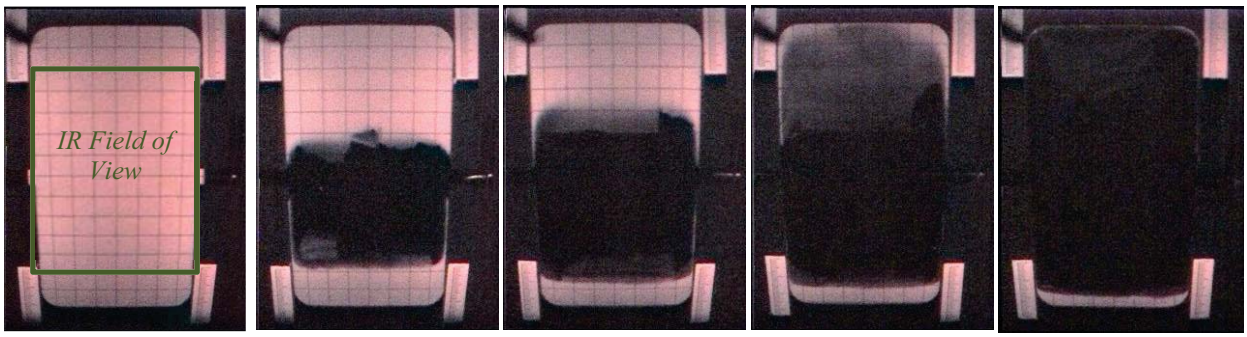

a) Unburned b) 2 cm/s c) 5 cm/s d) 10 cm/s e) 20 cm/s

Figure 3: a) Initial sample size showing IR field of view and b)-e) Post-test sample images showing char patterns. The samples were extinguished on impact using a CO2 jet into the chamber, so these char patterns reflect the 0g burn extent. Flow is from bottom to top in these images. As flow increases, the extent of char increases in both directions, but it increases more so for the downstream flame.

3.2 Blackbody Temperature Profiles

Blackbody surface temperature line profiles near the centerline down the length of the sample were taken every 0.5 second to study the transient surface temperature data. Figure 4 shows these line profiles from each case. The igniter location is at 0 cm. Upstream of the igniter (opposed flow flame region) is positive x, and downstream of the igniter (concurrent flow flame region) is negative x. The shaded box from 500K to 600K indicates where the temperature gradient (dT/dx) data was evaluated. This temperature range was selected to capture the preheating below the pyrolysis temperature. For example, notice in Figure 3c, the fuel pyrolysis extends downstream to about -3 cm. In Figure 4b, the temperature at -30 mm just reached 600K. The visible image in Fig. 3c reveals that the sample is darkened downstream of 30 mm, but not to the point where the printed grid is no longer visible. Temperatures at the 5th grid line (-50 mm) did not exceed 500K even though the sample continued to -70 mm (out of the IR field of view).

As seen in all four of the plots in Figure 4, there is a spike at x=0 corresponding to ignition. The upstream flame becomes very steady as shown by the similarity in the temperature profiles at different times. The surface temperature plateaus during pyrolysis at 650-700K. At 2 cm/s and 5 cm/s there is no peak for oxidative pyrolysis. Once burnout occurs, the surface temperatures drop, but not back to the baseline reading due to gas- phase radiation. There is a general increase in the gas-phase radiation with flow, due to increasing temperatures and soot (Figure 2).

Downstream profiles do not show the same steadiness. In Figure 4a and 4b, the profiles become more closely spaced as time increases. In Figure 4c, the profiles begin to show a uniform shifting later in the drop. Figure 4d shows a large fairly uniform spacing early, with the preheat region quickly moving out of the field of view of the IR camera (by 5 sec). There are large spikes in temperature at the flame base of the downstream flame in both Figure 4c for later profiles and more extensively in Figure 4d, indicating exothermic char oxidation is occurring there.

3.3 Temperature Gradients

The surface temperature gradients (dT/dx) as a function of time extracted from this data is shown in Figure 5. Error bars on the temperature gradient are estimated to be ±10% of the gradient, based upon the 20°C accuracy of the camera and the 100°C range for the gradient evaluation. The upstream temperature gradient reaches an approximately constant value after the ignition transient (~ 4 s). At low flows, the value of the temperature gradient does not change, indicating that conduction and diffusion are dominating the heat transfer and flame standoff distance. At higher flows, the temperature gradient increases, indicating that convection dominates the heat transfer from the flame.

The downstream temperature gradients are much lower, and only reach steady state levels of less than 6 K/mm for the higher flows. The average post-ignition temperature gradients are plotted in Figure 6. There is almost an order of magnitude difference between the upstream flame and the downstream flame. The fuel beneath the upstream flame heats up quickly due to the intense heat flux from the leading edge of the flame in contrast to the fuel beneath the downstream flame, which has a much larger standoff distance.

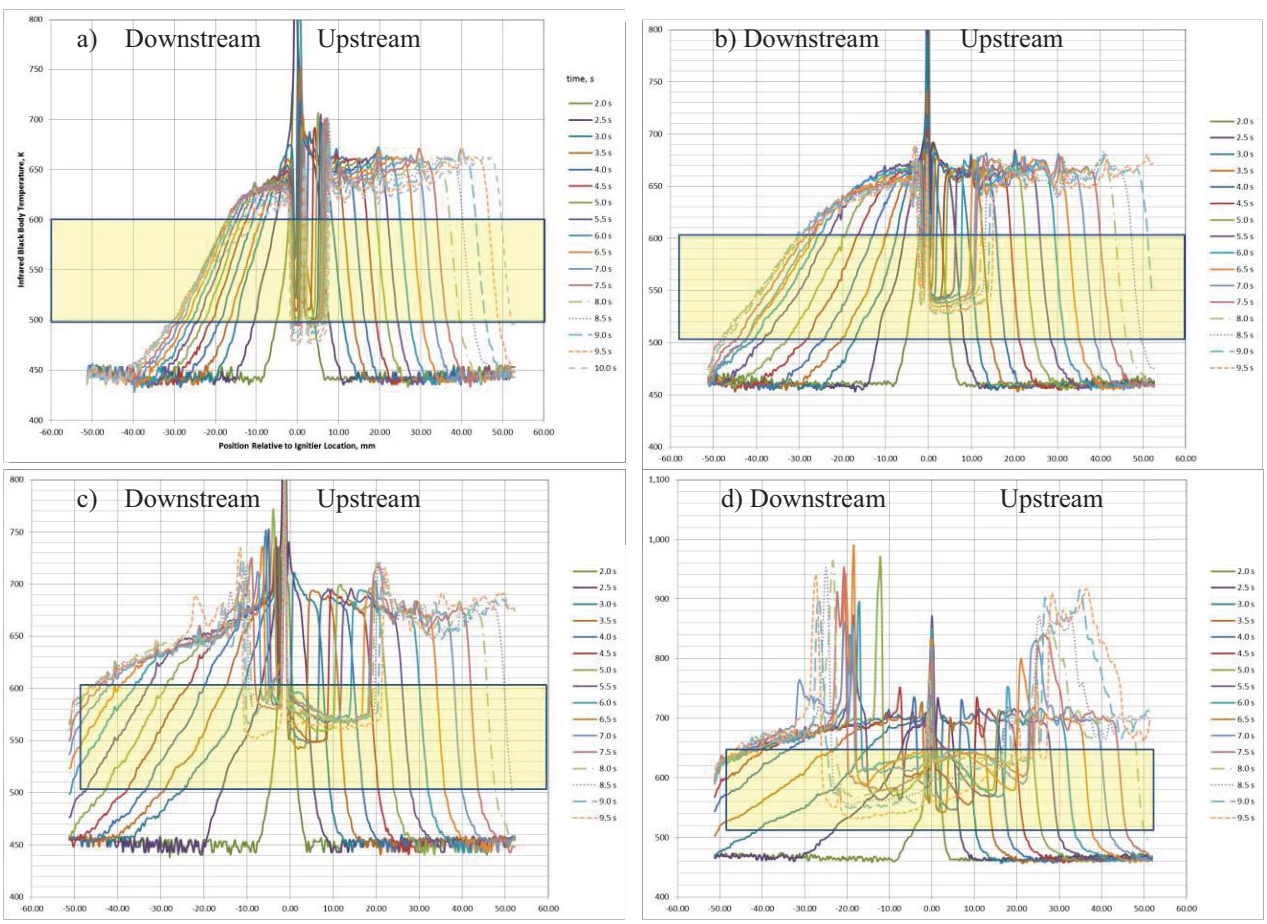

Figure 4: Blackbody surface temperature line profiles as a function of time for 35% O2, 1 atmosphere tests: a) 2 cm/s, b) 5 cm/s, c)10 cm/s, d) 20 cm/s. Yellow shaded box gives temperature range over which the temperature gradient was obtained.

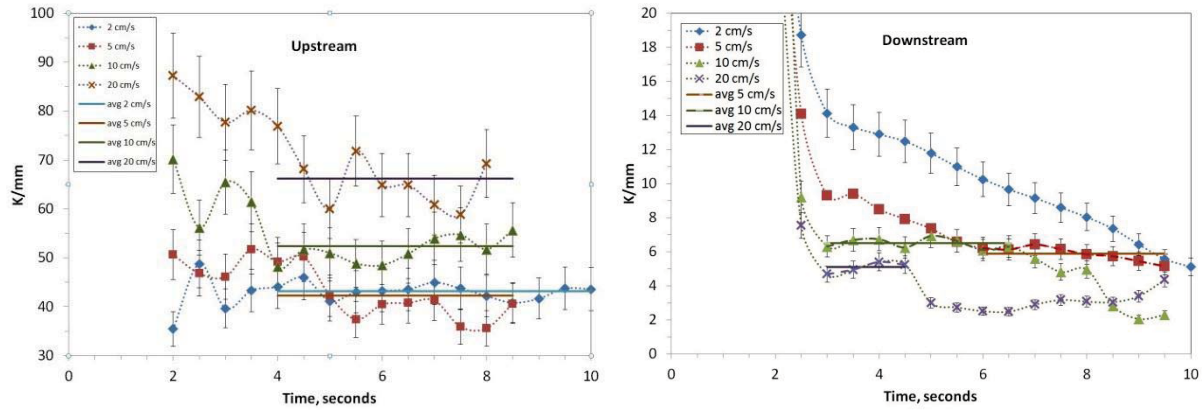

Figure 5: Temperature gradients for both upstream and downstream directions as a function of time during each microgravity drop with flow as indicated. a) upstream gradients, b) downstream gradients.

3.4 Flame Spread

The surface temperature can also be used to track the flame spread rate. To do this, we chose a surface temperature of 600K as a reasonable pyrolysis temperature. This worked well for the upstream flame spread and downstream flame pyrolysis tip spread, but the downstream flame base spread required a higher temperature (700K) to detect the base (burnout) of the flame. Figure 7 shows the pyrolysis position versus time data for each flow case for both the upstream and downstream data.

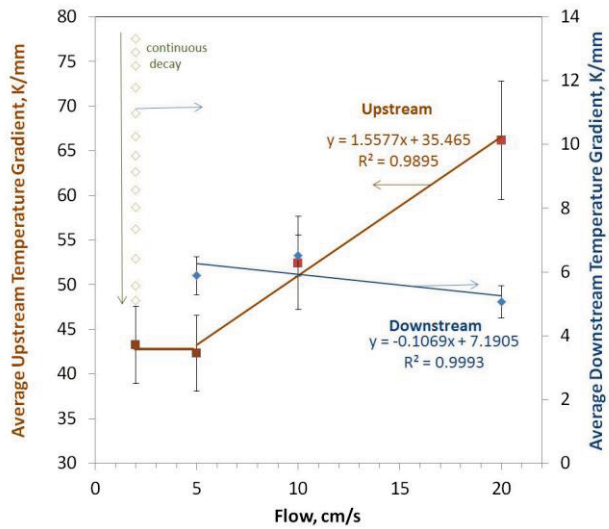

Figure 6: Average post-ignition transient temperature gradients for each flow condition. Downstream gradients are an order-of magnitude lower than upstream gradients, due to the different flame structure for the two flames.

The upstream flame spread is steady for each case, and linear fits to each position versus time curve are shown. The downstream flames take longer to stabilize than the upstream flames, and the downstream pyrolysis fronts (600K) spread rapidly as the flame grows from ignition.

The downstream flame base (700K isotherm) moves more slowly but steadily downstream for the higher flow rates. At 2 cm/s the pyrolysis front (600K isotherm) spread stops and the sample actually begins to cool as the upstream flame moves away. At 5 cm/s the pyrolysis front stops, but just starts to cool at the end of the drop. At 10 cm/s, the pyrolysis front slows but does continue to spread at approximately the same rate as the flame base (700K). The 20 cm/s case pyrolysis front begins to slow down, but does not reach a steady state pyrolysis front before the 600K isotherm moves outside of the IR camera field of view.

Flame spread rates derived from the slopes of the curve fits in Figure 7 are shown in Figure 8 as a function of flow. The upstream or opposed flow flame spread rate, increases at low flow, but

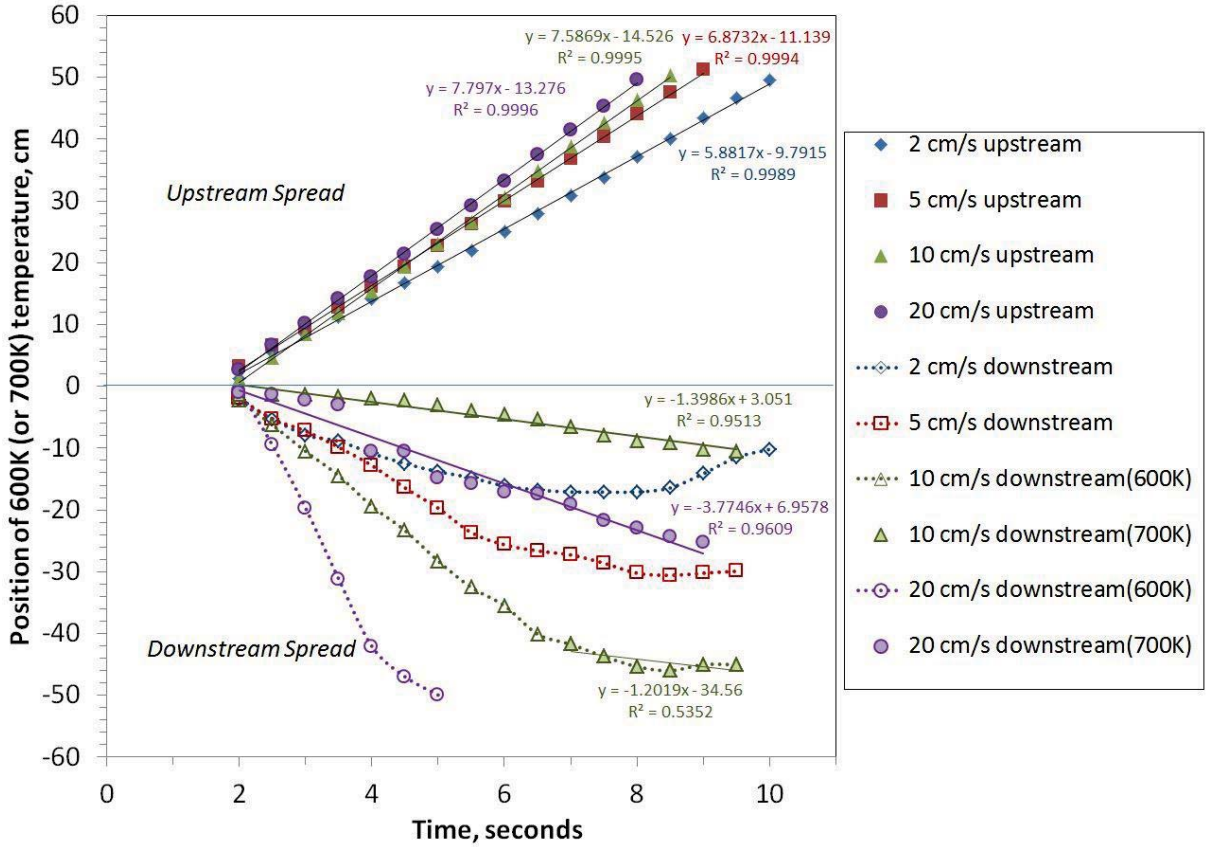

Figure 7: Position of the upstream 600K and downstream 600K and 700K thermal waves as a function of time. Downstream flames do not reach a steady length for the 20 cm/s flow case. Linear fits (shown) provide the flame or pyrolysis front spread rates.

plateaus at higher flow as conditions enter the thermal regime of flame spread [Olson (1991)]. This is consistent with previous research using visible imaging at this elevated 35% oxygen concentration [Prasad et al.].

The downstream spread of the flame base is also shown in Figure 8. The flame base spread rate increases linearly with flow, which is also consistent with prior research [Ferkul & T'ien]. At low flow rates, the downstream flame is not simultaneously viable with the upstream flame, due to oxygen vitiation from the upstream flame, despite significant heating and fuel surface pyrolysis in over the first few cm of the downstream sample.

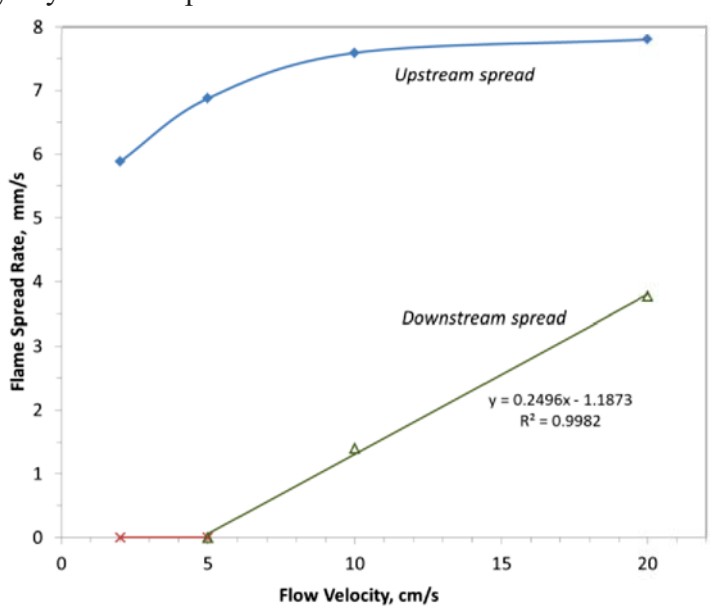

Figure 8: Flame spread rates for simultaneous opposed and concurrent spread as a function of the ambient flow. The upstream spread is the leading edge spread rate, and the downstream spread is the flame base spread rate. The downstream flame is not simultaneously viable for the the 2 cm/s and 5 cm/s flows.

3.5 Flame Preheat and Pyrolysis Lengths

The preheat lengths for the flames can be estimated by evaluating the length from ΔT=600K-300K (ambient to pyrolysis temperatures), based upon the measured linear temperature gradients shown in Figure 4 (i.e. 300K/(dT/dx)). For those downstream cases where flame base burnout was observed, pyrolysis lengths can be measured directly by locating the x locations for isotherms for 700K and 600K and taking the Δx between them. For upstream pyrolysis lengths, the Δx between the rising 600 K isotherm (leading edge) and the decaying 600K isotherm (burnout) can be used, as shown in Figure 4.The direct measurements are needed since the temperature gradients are not relevant in this temperature range. The calculated preheat and pyrolysis lengths are shown in Figure 9 for each case.

In each case, the upstream flames have a very small but steady preheat on the order of 5 mm. The upstream pyrolysis length grows with time for each case, never reaching steady state. However, the

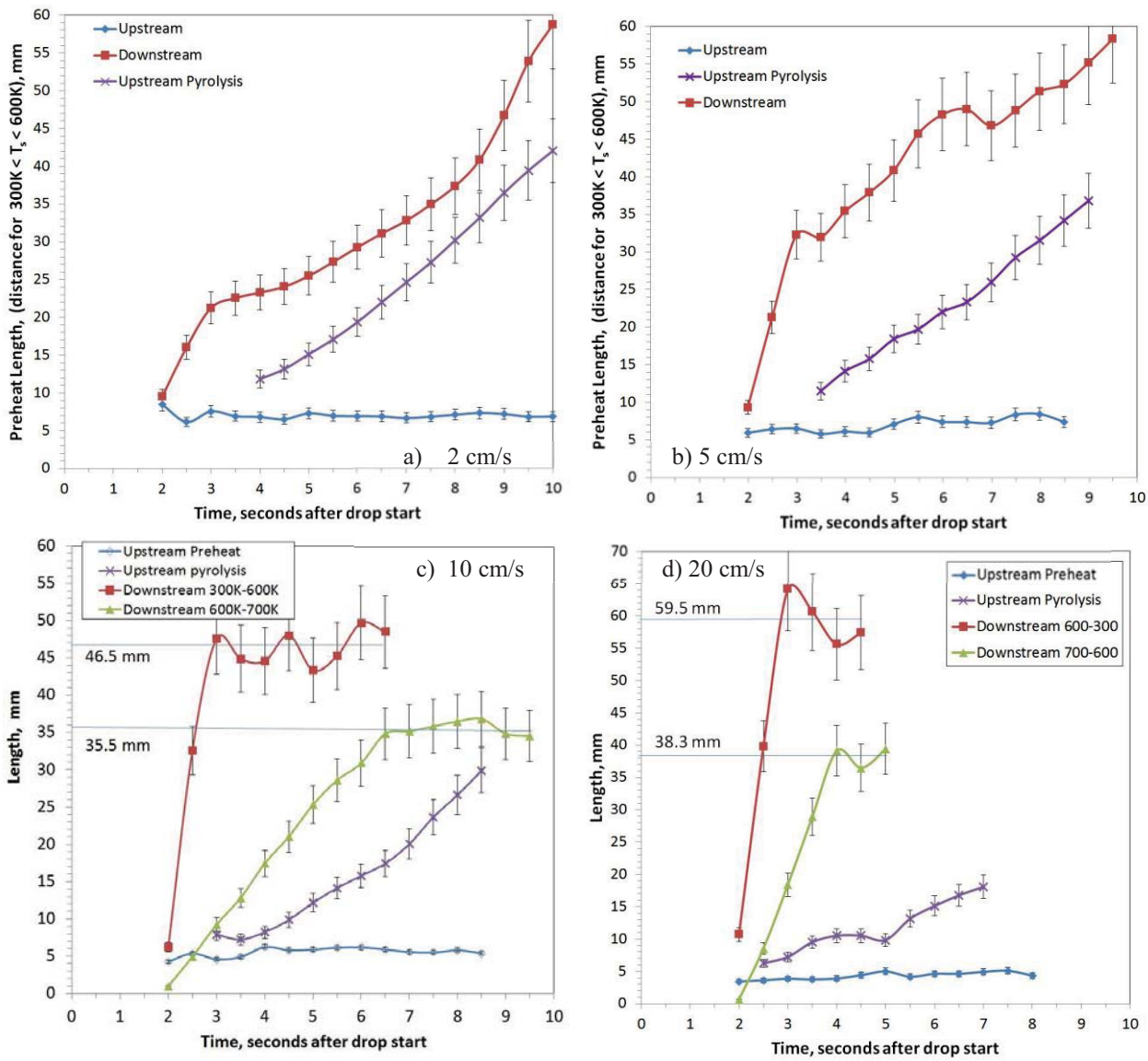

Figure 9: Preheat and Pyrolysis Lengths for each test. The preheat lengths are taken from 300K-600K, and pyrolysis lengths from 600K-700K. a) 2 cm/s; b) 5 cm/s; c) 10 cm/s; d)20 cm/s.

pyrolysis lengths are shorter at higher flow, as the fuel burns out sooner with the increased heat flux.

The downstream flame preheat length rapidly grows early in the test as the flame expands downstream. For the 2 cm/s and 5 cm/s cases, no steady preheat length is seen since the flame base does not propagate downstream in these cases and as the temperature gradient decays, the calculated preheat length continues to increase.

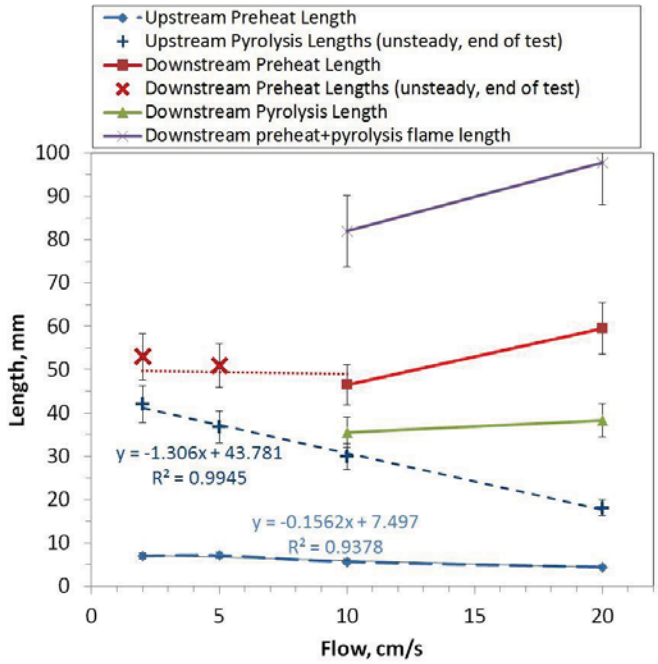

Figure 10: Preheat and Pyrolysis Lengths as a function of flow for both upstream and downstream flames, based on values from Figure 9.

For the 10 cm/s case, the downstream flame does grow and reaches a steady preheat length of ~46.5 mm until late in the test when the 600K line approaches the edge of the IR field of view. The downstream burnout front (flame base) is represented by a much higher temperature (700K), so we also directly measure the distance between 600K and 700K, which is also shown in Figure 5, and reaches a steady length of ~35.5 mm later in the test. To estimate the total preheat length from ambient to burnout, we add the two pseudo-steady values to estimate a pseudo-steady preheat length of ~84 mm for the downstream flame, which is longer than the actual downstream sample (70 mm), so an actual steady-state concurrent flame size was not obtained for this test. This is not surprising, since the downstream flame never full separated from the upstream flame.

For the 20 cm/s case, the downstream flame rapidly grows out of the IR field of view, so measurements are not complete. The measured preheat length was 59.5 mm, and the measured pyrolysis length was 38.3 mm, for a total length of 97.8 mm, much longer than the available sample.

Figure 10 has a summary of the measured flame lengths for the four cases. The upstream preheat lengths shown a decrease with increasing flow as would be expected from α/U scaling. The upstream pyrolysis lengths at the end of the test also exhibit a linear decrease with increasing flow. The end of test downstream preheat lengths at the lower flows are ~ 5 cm and do not vary with flow within the estimated error, but do show an increase for the 20 cm/s case. The downstream pyrolysis lengths can only be measured for the highest two cases since only for those cases did the temperatures reach 700 K after the ignition transient. The pyrolysis length is shorter than the preheat length for the downstream flame, in contrast with the upstream flame. The total downstream estimated flame lengths (preheat + pyrolysis) are also shown, but are longer than the actual sample so direct measures were not possible.

3.6 Thermocouple Readings

The thermocouple data for the surface thermocouples can be compared with the IR image results. The thermocouple data for the four cases is shown in Figure 11. In Figures 11a and 11b the upstream surface thermocouples at +2 cm and +4 cm are plotted for the four cases. In each test, the thermocouple heats up sharply in a convex shape from ambient as the flame approaches. The shape of the curve has an inflection point at the peak heat flux beneath the flame leading edge, and then the curve plateaus at the fuel pyrolysis temperature. These plateau pyrolysis temperatures are plotted in the inset as a function of flow. At the +2 cm location, the flame arrival time is nearly constant due to the proximity of the igniter. Interestingly, the slowest flows respond first to the approach despite the slower spread rate. This is attributed to the ~ 1.5x larger preheat distance at the slow flow compared to the fastest flow. The pyrolysis temperatures increase linearly with flow. At the +4 cm location, the difference in spread rates has allowed the faster flames to arrive earlier so the profiles stack with the flow. The pyrolysis temperatures are nearly identical to the +2 cm temperatures, indicating the upstream flame is steady.

Figure 11c shows the surface thermocouple data for -2cm for each of the four cases. The heat up occurs almost from ignition as the heated gas flows downstream past the thermocouple. The shape of the curve is nearly linear early on, and then plateaus out to pyrolysis temperatures. These are again plotted in the inset. The downstream pyrolysis temperatures are non-linear with flow, and lower than the upstream temperatures for the same flows.

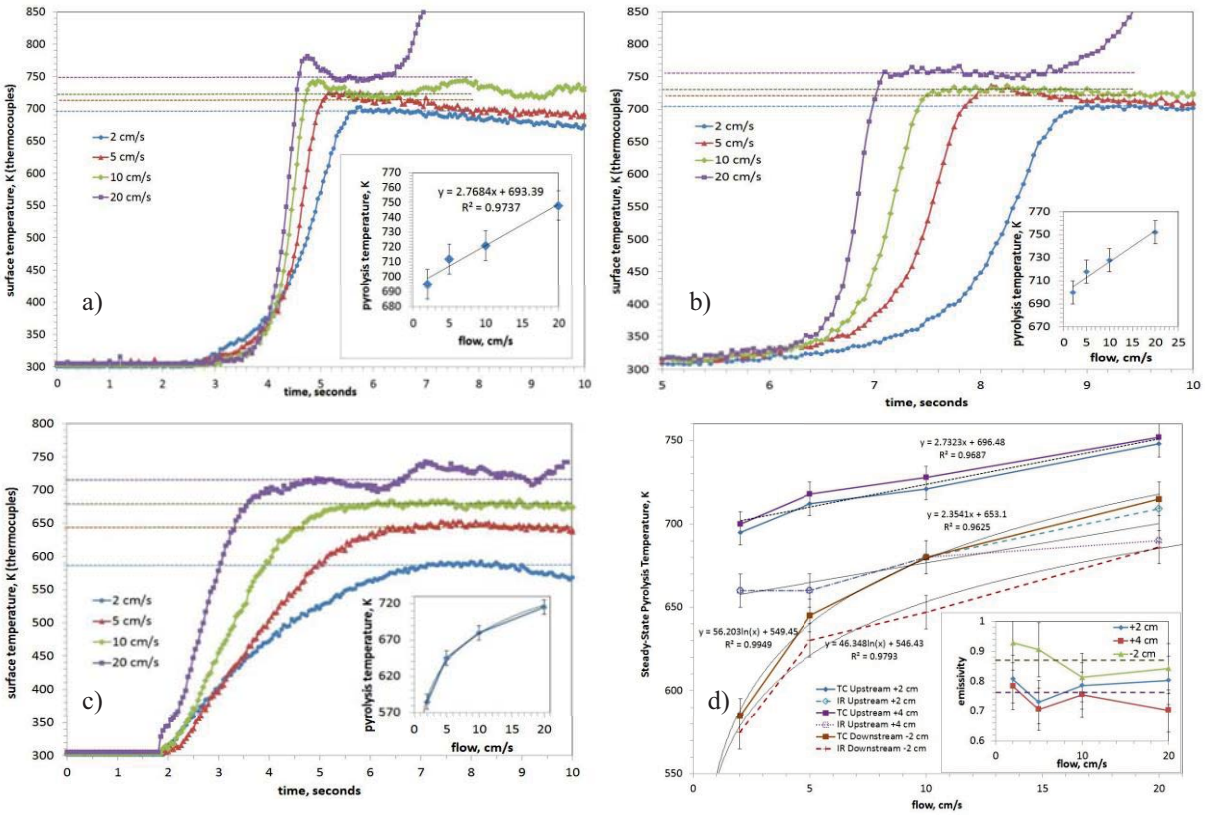

Figure 11: Surface thermocouple data for the 4 cases at 3 axial locations: a) +2 cm, b) +4 cm, and c) -2 cm. Insets in each figure show the trend in pyrolysis temperatures with flow. d) steady plateau pyrolysis temperatures for all cases as a function of flow, and compares these values to the IR plateau values. The inset shows the emissivity calculated from this comparison using Eqn. 1.

3.7 Surface Emissivity

Figure 11d plots the pyrolysis temperature data for the 3 locations and compares it with the IR blackbody pyrolysis temperatures at the same X locations. The trends with flow are the same, but the blackbody temperatures are always lower. A comparison can be made to determine the emissivity of the pyrolyzing surface for the wavelength range of the flame filter. By definition, comparing thermocouple measurements with blackbody IR temperatures (ε=1) readings the surface emissivity is:

$$\varepsilon = \frac{T_{IR}^4 - 300^4}{T_{TC}^4 - 300^4} \quad (1)$$

The estimated average emissivities are shown as dashed lines: 0.76 for the upstream pyrolyzing fuel and 0.87 for the downstream pyrolyzing fuel. The variation with flow is within the error estimate (±10%, based on IR temperature error estimates), but the differences between upstream and downstream emissivities is slightly larger than this error, and the downstream emissivity is consistently higher. This may be due to the prolonged preheating of the downstream fuel over the large preheat length that allows a more thorough pyrolysis of the fuel.

3.8 Energy Balance

An energy balance can be used to evaluate the net heat flux from the flame (which includes convection and radiation) to the fuel surface, neglecting the heat of pyrolysis. The energy balance for the fuel is

$$\dot{q}''_{net\,flame\,heat\,flux} = \rho_s \tau C_s \frac{\partial T_s}{\partial t} + \varepsilon\sigma (T_s^4 - T_\infty^4) \qquad (2)$$

Where $\rho_s\tau$ is the cellulose fuel half-area density of 0.003 g/cm^2, C_s is the fuel heat capacity, 1.26 J/g K, ε is the emissivity, which is unity for these black body temperature measurements, and σ is the Stefan-Boltzmann constant (5.729x10^{-12} W/cm^2 K^4). T_s is the blackbody surface temperature in K, and ambient temperature T_∞ is 300K. The time derivative in surface temperature is evaluated by simple difference over a 0.5 second interval at each pixel location along the line profile.

Figure 12 shows the resulting heat flux profiles for the four flow cases at 35% O_2. The profiles stop at ~0.2 W/cm^2 at the low end of the IR operating temperature range of ~450K. Figure 13 plots representative profiles relative to the peak heat flux for each flow. The upstream flame transitions from the ignition to a steady-state leading edge peak heat flux followed by a plateau at about 1 W/cm2 for pyrolysis.

The downstream flame has a peak at burnout, and a long low level preheat beneath the flame. The low level of downstream heat flux is due to the large flame standoff distance. The burnout peak heat flux is only an estimate, since the pyrolysis term was neglected in the estimate and there is clearly exothermic oxidative pyrolysis occurring at burnout at the 20 cm/s flow. Also, a significant portion of the fuel surface above the pyrolysis temperature (~600K), as shown in Figure 4, especially at the higher flows. At these low levels of heat flux beneath the downstream flame, and the

extensive length of elevated temperature surface, radiative loss is a much more significant term than for the upstream flame.

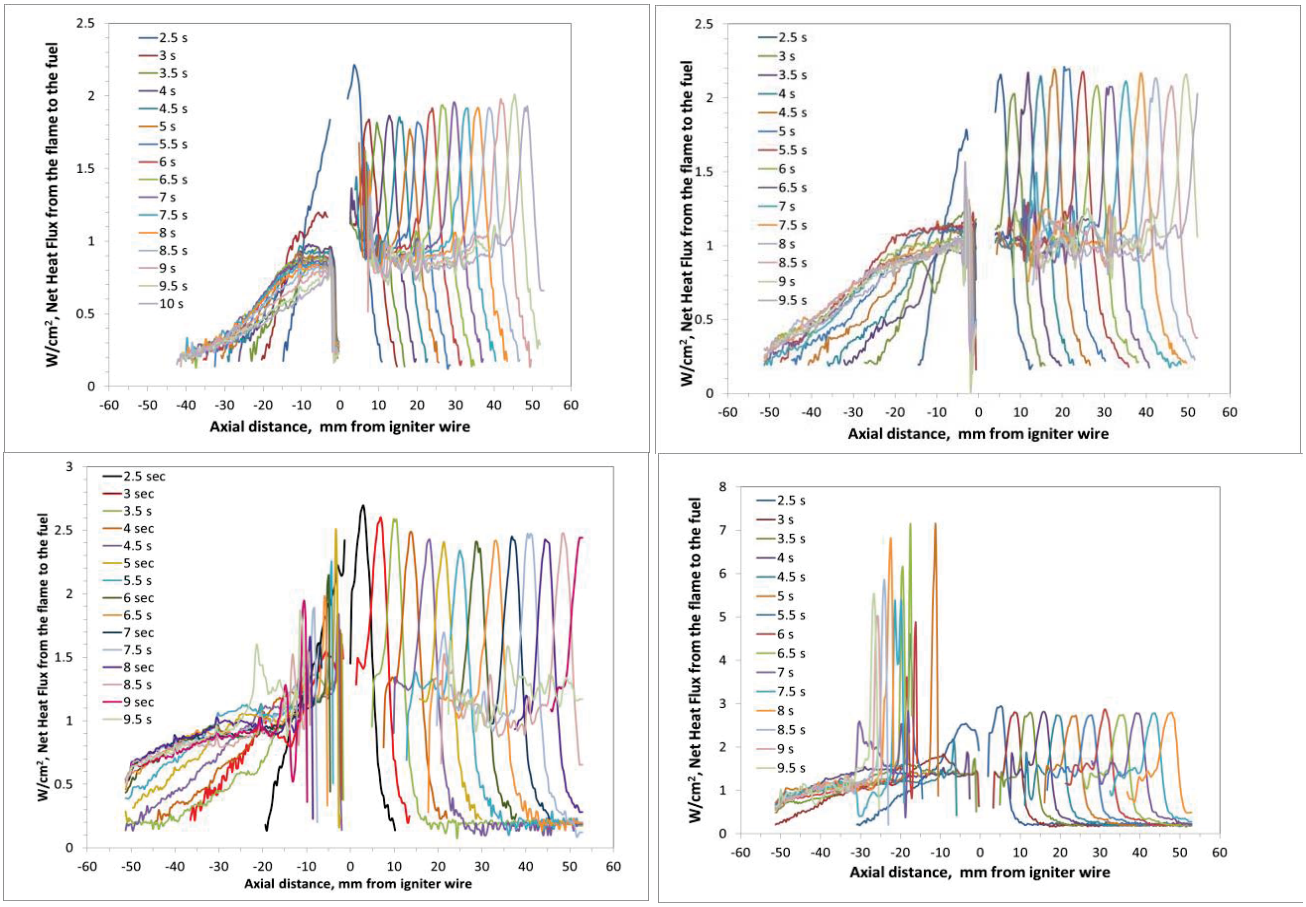

Figure 12: Flame net heat feedback to the fuel surface based on the energy balance, Eq. (2). a) 2 cm/s, b) 5 cm/s, c)10 cm/s, d) 20 cm/s.

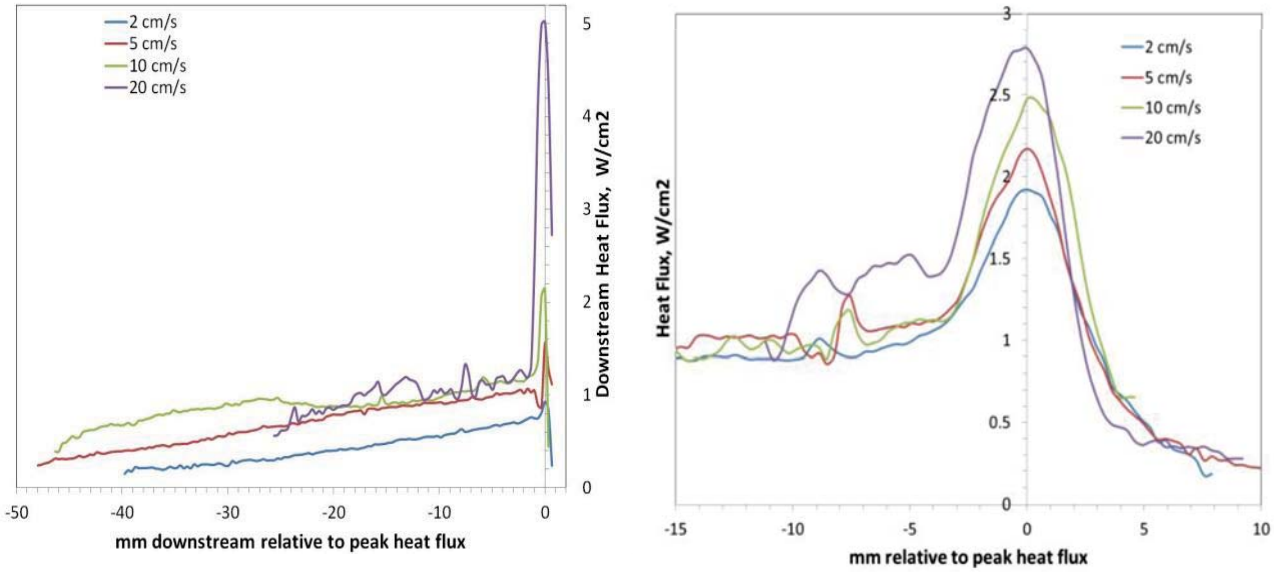

Figure 13: Representative heat flux profiles plotted relative to the peak location for a) downstream flame and b) upstream flame.

The peak heat flux was extracted from the data and is plotted in Figure 14. Figure 14a shows the steadiness of the upstream peak heat flux as a function of time. In Figure 14b the downstream flame peaks at 20 cm/s vary considerably with time, which is attributed to the very sharp peak in the very small burnout zone. Figure 14c takes the average values of the heat flux and plots them as a function of the flow. The upstream heat flux increases linearly with flow, whereas the downstream heat flux increases gradually at low flow, and is actually lower than for the upstream flame. At 10 cm/s when the downstream flame begins to spread, the heat flux increases more rapidly. The error bars represent the standard error of the data sets.

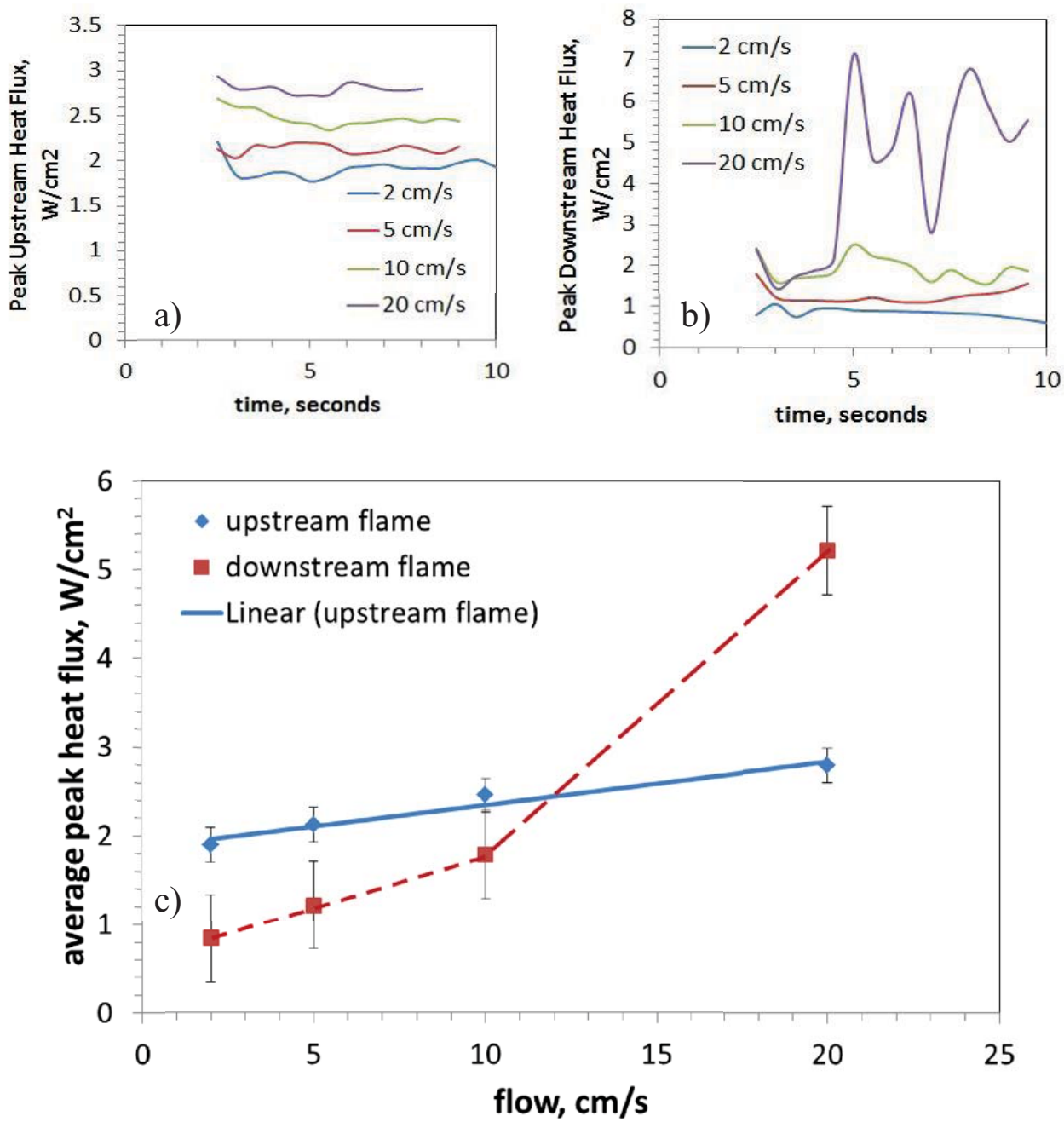

Figure 14: Peak heat flux levels a) upstream flame as a function of time; b) downstream flame as a function of time; c) average peak heat flux versus flow for both upstream and downstream flames.

3.9 Radiative heat transfer

3.9.1 Surface Radiative Heat Loss

The fraction of heat lost via surface radiative loss can be estimated using an average blackbody pyrolysis temperature of T_s=650K:

$$loss\ \ fraction = \frac{\sigma(T_s^4 - T_\infty^4)}{\dot{q}''_{net\ flame\ heat\ flux}} \quad (3)$$

The radiative heat loss for this temperature is 0.98 W/cm^2. The average peak heat flux levels from Figure 14c are used for the net flame heat flux values. The loss fraction is plotted in Figure 15. The loss fraction drops with increasing flow as one would expect. The upstream loss fraction changes only slightly, but the downstream losses increase significantly at low flow. For the two non-propagating downstream flames, the losses exceed 70%, consistent with [Olson et al. (2001)].

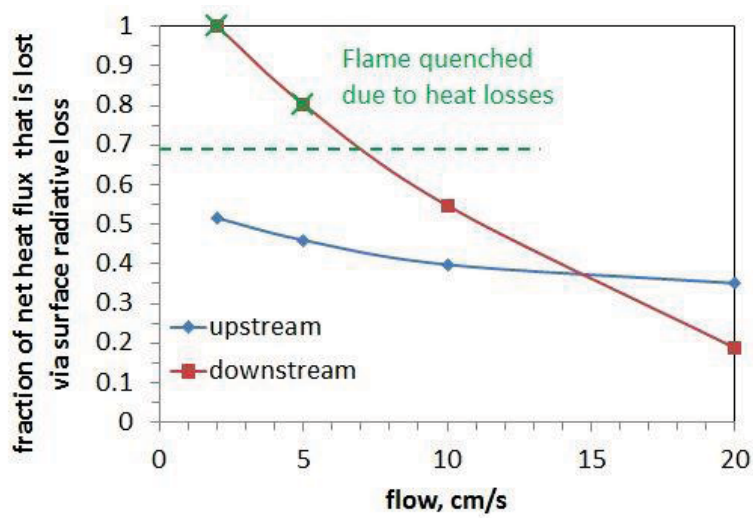

Figure 15: Estimated radiative loss fraction for the upstream and downstream flames. For losses greater than 70%, no downstream flame propagation is observed.

3.9.2 Gas-Phase Radiation

The gas phase radiation can also be estimated from the IR images in the gap where the fuel has burned away. The emissions are primarily from soot at 3.8 microns, and we can directly calculate the gas-phase radiation from the blackbody temperatures and the floor temperature of the IR camera of 450K:

$$\dot{q}''_{gas-phase} = \sigma(T_g^4 - T_{IRfloor}^4) \quad (4)$$

The temperatures were taken at +3 mm once the fuel burned away. The radiant flux is plotted in Figure 16 as a function of time. For 2 cm/s and 5 cm/s the radiation does not change significantly with time, and just exhibits a gradual decline as the flame moves upstream. At 10 cm/s and more so at 20 cm/s there is an increase in gas-phase radiation as the leading edge of the flame moves away, and then a decline after a peak in radiation as the peak sooting zone moves upstream as well. Figure 2 visible front views show that at 20 cm/s the soot zone is mostly upstream of the igniter location. The inset to Figure 16 plots the peak values and average values as a function of flow. Both show a linear increase with flow.

The gas-phase radiation can be a heat loss mechanism (especially for opposed flow where the view-factors are poor for preheating the unburned fuel) or a heat feedback to the fuel, which is significant for the downstream flame preheating. To estimate the relative importance of the flame feedback on the flame spread, we take the ratio of average gas-phase radiation to the net flame heat flux. For the upstream flame, the peak heat flux at the leading edge is used, but for the downstream flame, the pre-peak heat flux was used because we want to assess the importance of gas-phase radiation for preheating and pyrolysis rather than burnout, where the peak flux occurs. The gas-phase fraction data are plotted in Figure 17 for upstream and downstream flames. For the upstream flame, gas-phase radiative feedback at the leading edge is at most 20% of the net flux, but for downstream flame it exceeds 30% of the feedback for those cases where the downstream flame was viable. It is thus a significant factor in the viability of the downstream flame.

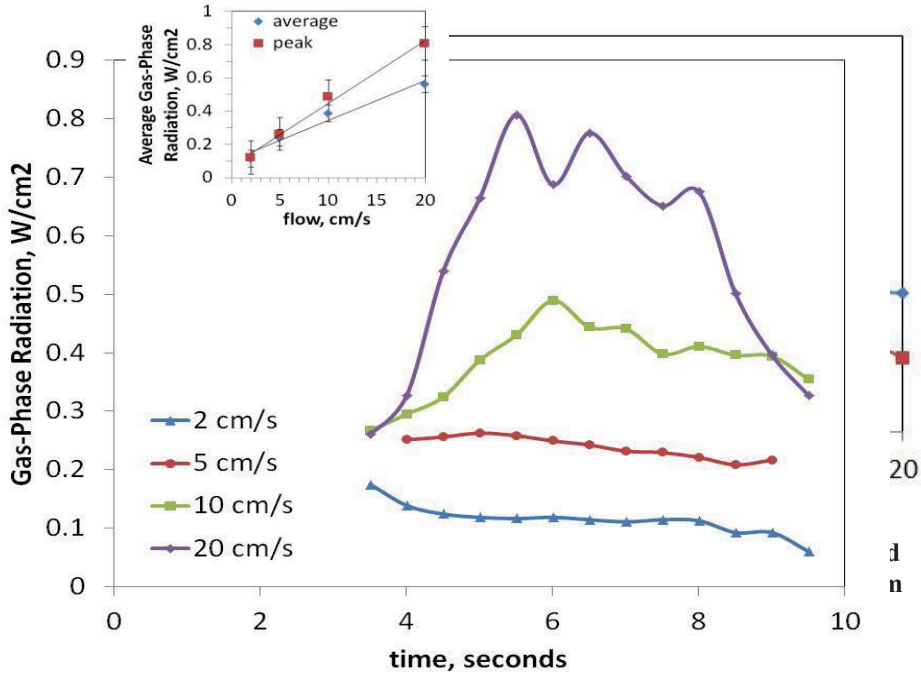

Figure 16: Gas-phase radiation estimates in the burnout gap as a function of time and (inset) average values as a function of flow.

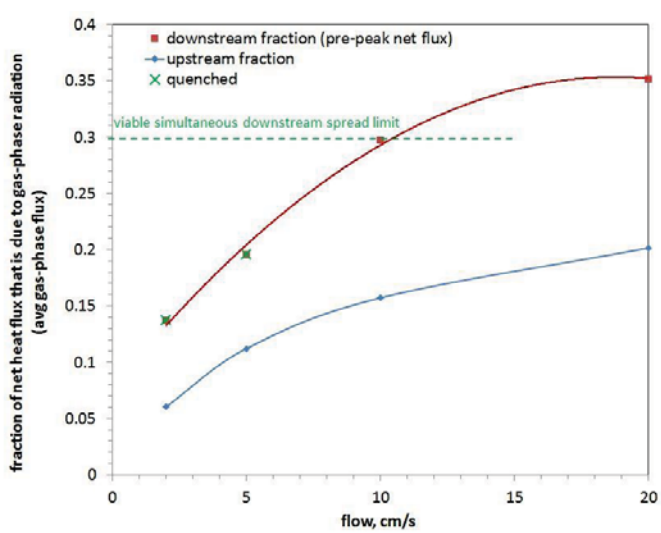

Figure 17: Fraction of the net flame heat flux that is attributed to gas-phase radiation to the upstream leading edge of the flame or the downstream preheating / pyrolysis.

The relative magnitude of the surface loss (~ 1 W/cm^2) and the gas-phase radiation feedback is interesting for the downstream flame. Comparing this loss to the values in the inset to Figure 16 show that at low flow rates, where convective heat transfer is weak, the gas-phase radiation is only ~ 15-30% of the surface loss, so the losses dominate and the downstream flame is not viable. At higher flow rates the gas-phase feedback approaches the level of the surface loss, thus counteracting this loss to a large degree (up to 80%), and the flames are viable.

The 10 cm/s flow case is a borderline case for downstream spread. The peak heat flux is 1.8

W/cm^2, and of that, the gas-phase feedback is an average of 0.4 W/cm^2. Therefore, the convective heat flux is approximately 1.4 W/cm^2. The peak heat flux is still slightly less than the 2 cm/s upstream flame which had a peak heat flux of 1.9 W/cm^2. By 20 cm/s the downstream peak heat flux is 5.2 W/cm^2 and gas radiation feedback is a peak of 0.8 W/cm^2, so the convective component is 4.4 W/cm^2. At 5 cm/s, in contrast, the peak flux is only 1.2 W/cm^2, and the radiative feedback is 0.2 W/cm^2 of that. Convective flux is thus on the same order as the surface radiative loss, and the downstream flame is not viable.

4. Discussion

Infrared imaging has been shown in the preceding sections to be a very useful quantitative diagnostic to measure many aspects of flame spread and heat transfer in the flame zone. The shorter wavelength IR camera is particularly well suited to measure the range of burning surface temperatures. The flame filter at 3.8 microns eliminates most of the gas-phase radiation except soot. Preheat and pyrolysis lengths are determined directly from the IR images in section 3.5. These lengths can be very hard to determine from visible imaging, and usually at least 2 orthogonal views are required.

The upstream spread rates in section 3.4 agree well with the visible spread rate measurements [Olson et al. (2001), Prasad et al.], and the infrared measurement are expected to be more reliable since the visible flame is very luminous and increases in brightness as the test progresses and the burnout gap grows in time. Comparison with the model predictions for this same experimental configuration and test conditions [Prasad et al.], shows that the model predicts a weaker flame than is experimentally observed. At 1.5 cm/s, the model predicts a flamelet (3D), whereas at 2 cm/s the experiment exhibits a steady planar upstream flame spread across the full sample. At 10 cm/s the model predicts that the downstream spread will occur along the edges. A similar type of spread was in fact observed at 5 cm/s in air [Olson et al. (2001)] where an upstream flame spread away from a central ignition spot and, after spreading to the upstream edge of the sample, wrapped back around along the edges to form a downstream flame spread. In this paper, at 10 cm/s, 35% O2, the downstream flame is spreading along the entire sample width. At 20 cm/s, both model and experiment observe flame separation and subsequent two simultaneously propagating flames.

The heat flux estimates from the infrared measurements in section 3.8 are better than those based on the thermocouple data, which needed to be smoothed and differentiated [Olson et al. (2001)]. In contrast, simple finite differencing is used here. Comparison with these previous estimates for 35% O2 tests shows that the linear increase with flow trend is the same, but the magnitude of the upstream heat flux is lower via the infrared measurements.

Quantitative heat flux estimates for upward and downward spread over thick cast PMMA using holographic interferometry [Ito and Kashiwagi (1988)] agree in general trends presented here, but the magnitude of the heat flux is different for this thick material. For downward spread, they found the peak heat flux increased rapidly to 7 W/cm^2 within a short 3.4 mm of preheating, and for upward spread they found a much lower gradually increasing heat flux over approximately 5 cm of sample that reaches 2.8 W/cm2 at the vaporization front (burnout is not reported for this thick material). These length scales and relative peak values (factor of ~2.5 for upstream to downstream) agree with those seen in Figure 13, except the for the burnout peak flux for the downstream flame.

5. Conclusions

The infrared surface temperature image data obtained during microgravity testing of cellulose ignition and flame spread have been analyzed to provide quantitative temperature gradients, preheat lengths, flame spread rates, and net flame heat flux to the fuel sample for simultaneous upstream and downstream flame spread. Four cases have been examined that range from upstream only spread to a clearly simultaneous upstream and downstream flame spread. The results highlight the differences in the structure of the two halves of the flame as they spread apart. Upstream flame spread is controlled by the leading edge of the flame. Net heat flux increases with increasing flow, as does the flame spread rate. Downstream flames have very long preheat lengths with a very low heat flux, and are at higher flow rates are anchored to the fuel at the flame base which provides a sharp spike in the heat flux to consume the fuel. At low flow rates the downstream flame is not viable due to the low heating rate and the significant radiative losses. The infrared surface temperature data reported here can provide added depth to the model comparisons.

6. Acknowledgements

This work was jointly supported by a NASA/ NEDO international agreement. The microgravity experiments of this work were performed at JAMIC (Japan Microgravity Center) during March, 1999 under the management of JSUP (Japan Space Utilization Promotion Center) as a part of an R&D project of advanced combustion science utilizing microgravity by NEDO (New Energy and Industrial Technology Development Organization of Japan). The authors would like to thank NASA electrical engineer Mike Capelety and the NASA TIGER engineering team for supporting the rig buildup and testing. The authors would also like to thank Kenichi Ito, Katsuhiro Nishizawa and JAMIC facility personnel in performing the microgravity experiments.

7. References

Bhattacharjee, S., Altenkirch, R.A., Olson, S.L., and Sotos, R.G.; J. Heat Transfer 113 (3), 670-676, 1991.

Cordova, J.L., Walther, D.C., Torero, J.L., and Fernandez-Pello, A.C., Combust. Sci. and Tech. 164 (1) 253-278, 2001.

Di Blasi, *Combust. Flame* 100, 332-340, 1995.

Feier, I. I., Shih, H.-Y., Sacksteder, K.R., and T'ien, J.S.; Proc. Comb. Inst. 29 (2002), 2569-2577.

Ferkul, P.V., and T'ien, J.S.; *Combust. Sci and Tech.* 99 345-370, 1994.

Fernandez-Pello, A.C., Combustion Fundamentals of Fire, Chapter 2 "The Solid Phase", Academic Press Limited, 1995.

Hirano, T., and Saito, K.; *Prog. Energy Combust. Sci*. 20, 461-485, 1994.

Hirano, T., Noreikis, S.E., and Waterman, T.E.; *Combust. Flame* 23, 83-96, 1974.

Ito, A., and Kashiwagi, T.; *Combust. Flame* 71, 189-204, 1988.

Kleinhenz, J., Ferkul, P., Pettegrew, R., Sacksteder, K.R., and T'ien, J.S.; Fire & Materials 29 (2005), 27-37.

Kumar, A., Shih, H.-Y., and T'ien, J.S.; Combust. Flame 132, 667-677, 2003.

Olson, S.L., *Combustion Science and Technology*, 76,4-6, pp. 233-249, 1991.

Olson, S.L., Kashiwagi, T., Fujita, O., Kikuchi, M., and Ito, K.; Combust. Flame 125, 852-864, 2001.

Olson, S.L., Hegde, U., Bhattacharjee, S., Deering, J.L. Tang, L., and Altenkirch, R.A.; Combust. Sci. and Tech. 176, 557-584, 2004.

Nakamura, Y., Kashiwagi, T., McGrattan, K.B., and Baum, H.R.; Combust. Flame 130, 307-321, 2002.

Prasad, K., Nakamura, Y., Olson, S.L., Fujita, O., Nishizawa, K., Ito, K., and Kashiwagi, T., Proc. Comb. Inst. 29 (2002) 2553-2560.

Quintiere, J.G.; Fundamentals of Fire Phenomena, John Wiley and Sons Ltd., 2006.

Ross, H.D., ed. Microgravity Combustion: Fire in Free Fall, Academic Press, 2001.

Ross, H. D. and. Miller, F. J. *Twenty-sixth International Symposium on Combustion*, 1327–1334. Combustion Institute, 1996.

Sanchez-Tarifa, C. and Lazaro, B., First International Symposium on Microgravity Research and Applications on Physical Sciences and Biotechnology, 2000.

T'ien, J. S., *Combust. Flame* 65:31–34 (1986).